Geomechanics for Energy and the Environment 36 (2023) 100493

Contents lists available at ScienceDirect

Geomechanics for Energy and the Environment

journal homepage: www.elsevier.com/locate/gete

Landslide susceptibility evaluation in Alpine environment: 1. 3D Finite Element modeling of the Ruinon (IT) case study

Andrea Morcioni [a,*], Tiziana Apuani [a], Francesco Cecinato [a], Manolis Veveakis [b]

[a] Università degli Studi di Milano, Dipartimento di Scienze della Terra "Ardito Desio", via Mangiagalli 34, 20133 Milano, Italy
[b] Duke University, Civil and Environmental Engineering Department, Durham, NC, USA

ARTICLE INFO

Article history:
Received 2 June 2023
Received in revised form 30 August 2023
Accepted 30 August 2023
Available online 6 September 2023

Editors-in-Chief:
Professor Lyesse Laloui and Professor Tomasz Hueckel

Keywords:
Finite element modeling
MOOSE
Landslide susceptibility
Italian Alps

ABSTRACT

This manuscript is Part 1 of two companion papers that explore a multidisciplinary approach to predict velocity and stability of a large landslide located in the Central Italian Alps: the Ruinon landslide. The area is of high geological interest due to the presence of numerous shallow and deep gravitational instability processes that affect valley flanks, mainly driven by unfavorable morphological conditions and geomechanical properties of rock masses. In this manuscript, a 3D finite element model (FEM) was implemented in order to analyze the stress–strain distribution along the Ruinon rock-slope. Goals are to define the relation between morphological factors, mechanical parameters and the development of irreversible strains. The model was defined based on morphological features and mechanical properties detected along the slope, as well as on piezometric data from the landslide monitoring system. In a first step of the analysis, a static simulation was carried out under dry conditions. Then, a validation process was performed by comparing numerical outputs with geomorphological field observations. Finally, a parametric analysis was carried out where different piezometric level scenarios were evaluated in order to assess the influence of both mechanical parameters and pore pressure on the distribution of high sliding susceptibility areas. By overlaying satellite images with the model outputs, results were shown to accurately reproduce the extent of the slope areas subject to active gravitational instability. Parametric analyses showed a clear relationship between the input factors and the magnitude of strain, while the extension of areas subject to irreversible deformation did not change significantly. Stress distribution and stress–strain relations defined in this article are subsequently introduced in a thermo-hydro-mechanical (THM) numerical model presented in Part 2 of this work, where the evolution of the Ruinon landside is simulated.

1. Introduction

In recent years, an increase in the occurrence of landslide events in the Alpine region has been observed, mainly related to an extremization of climate variables.[1,2] The interaction with human activities drove local administrations and scientific communities to increase their interest in the analysis and management of these natural processes.

Landslide forecast is very challenging since their occurrence is related to both internal (e.g. material type, in situ stresses, geometrical and mechanical fracture network features) and external factors (e.g. intense rainfall events, snowmelt, freeze-thaw cycles), which are extremely variable over space and time.[3] In the past few decades, several authors have proposed a number of studies, both at regional and local scales, regarding the effect of climatic factors on the occurrence of landslides.[4–7] Inspection of the relevant bibliography, however, reveals the lack of common criteria and comprehensive procedural schemes for the spatiotemporal analysis and modeling of landslides (initiation, reactivation, and runout). The issue concerns not only shallow landslides, whose climate control is better understood, but also large landslides and rock avalanches, where the large volumes involved imply a high damage potential of these processes. Therefore, risk management is crucial since preventive actions (e.g., stabilization of entire slopes, effective defense works) are in most cases technically and/or economically unfeasible. The first step toward the prevention and mitigation of landslide risk is to identify the areas most prone to gravitational instability, that is, where the hazard is higher, and human activities are exposed to greater risk. Landslide susceptibility and hazard mapping have been based on the analysis of past landslide phenomena (inventory maps) and historical climate series (mainly rainfall). Within this framework, several approaches have been outlined that can be classified into: statistical,[8–11] deterministic[12–15] and numerical.[16–20]

* Corresponding author.
E-mail address: andrea.morcioni@unimi.it (A. Morcioni).

https://doi.org/10.1016/j.gete.2023.100493

Over large areas, statistical and machine learning methods are the most widely used, assuming landslide occurrence as a function derived from a combination of predictive factors such as morphological, land-use and geological features. Only recently, climate factors have been introduced as predictors to develop non-stationary landslide susceptibility maps.[21–24] The resulting algorithms aim to search for the optimal relationships that link the independent variables (morphology, land use, geology, climate) to the dependent ones (landslide occurrence). Through them, it is possible to quantitatively and objectively assess the impact of each parameter on the occurrence of known gravitational instability events along space and time. These methods, however, do not directly account for the physical laws governing the initiation and development of instabilities and crucial factors such as stress distribution, pore pressures, material properties and external loads are not investigated. Moreover, statistical approaches are not verifiable under important changes in the driving factors: the conditions responsible for observed landslide phenomena may in the future no longer exist,[25–27] especially in the context of ongoing climate change and other emerging scenarios. When applied outside its training range, a predictive statistical model is forced to work in an extrapolation scenario and, therefore, may lead to inaccurate results.

Deterministic methods provide quantitative information on landslide hazard by calculating the factor of safety for each map unit in order to plot its spatial distribution.[28–31] The factor of safety is defined as the ratio of resisting forces to driving forces acting along a potential failure surface, and is usually calculated through the limit equilibrium (LE) formulation (e.g. Refs. 32–34). Stability analyses by limit equilibrium methods have been performed generally by considering the plane strain assumption, adopting a 2D cross-section of the slope taken as representative of the real case. However, slope failures occur in three dimensions, and the significance of this difference, cannot always be neglected. LE methods require a simplified topographic surface geometry that does not allow evaluation of the role of morphology in stress distribution, which is of primary importance in natural slopes. The increased number of publications describing three-dimensional approaches, has motivated some scientists to make comparisons between two- and three-dimensional methods, typically resulting in a higher factor of safety for 3D analyses (e.g., Ref. 35). In addition, this approach has little applicability in defining landslide hazard over large areas, due to geological and mechanical variability of natural systems, that cannot be easily accounted for. Deterministic methods are widely employed to solve geotechnical engineering problems at the slope scale, finding good acceptance in the practitioner community over the years, through the development of different numerical software.[20,36–38] Despite its inherent limitations and a large number of simplifying assumptions, due to its simplicity, computational speed and ease of programming, the LE method is one of the most widely used deterministic approaches for geoengineering remediation.

Numerical techniques represent a good alternative to quantify slope stability and simulate slope stress–strain evolution under different external loads. Several authors adopted numerical techniques (based either on continuum or discontinuum formulations) to solve complex problems of slope stability, notably using Strength Reduction Techniques (e.g., Refs. 19, 39–41) that allow to quantify the stability of a slope with a factor of safety. The finite element method (FEM), represents a powerful and versatile alternative approach to LE slope stability analysis. While in the latter, only global equilibrium equations and (interface) constitutive laws are enforced, the former allows to achieve an exact solution of the mechanical problem, by also accounting for compatibility equations, thereby allowing to calculate internal strains and displacements. In addition, with the advancement in computing capabilities, the development of 3D FEM simulations requires reasonable computational costs even on large models, allowing the topographic factor to be included in the analysis of natural slope stabilities.[40,42,43]

This manuscript is Part 1 of two companion papers that explore a multidisciplinary approach to define a time-dependent slope stability criterion, that links the external forcing of a landslide with its internal response, to forecast its stability and velocity by identifying critical values, which can be measured in the field. In this work, a 3D FEM numerical model was implemented to analyze the stress–strain distribution along an Alpine slope, where an active landslide is located (Ruinon landslide, Sondrio Province, Italy). This work aims to define the relationship between morphological factors, mechanical parameters, and the development of irreversible strains. This analysis also aims to evaluate the most prone areas to gravitational instability, by using numerical stress–strain methods that incorporate the morphology of the slope, the strength properties of the geological medium, and the gravity factor. Because of its simplicity and the limited number of parameters required by the analysis, this tool may represent a valuable approach for landslide risk assessment and the installation and implementation of monitoring systems in areas of known instability.

The presented model was validated by comparing numerical outputs with morphological field observations, by focusing on the geometric elements of the landslide bodies detected in the region (depth of the sliding surface and location of irreversible deformations). A parametric analysis was carried out, and different piezometric level scenarios were evaluated to assess the influence of both mechanical parameters and pore pressure on the distribution of high sliding susceptibility areas in the model.

In the companion (Part 2) paper,[44] the stress–strain distribution calculated via FEM modeling in this work, is implemented into a thermo-hydro-mechanical (THM) mathematical model, where the stability and the velocity evolution of the Ruinon landside are simulated.

The paper is structured as follows. First, the study area is described by focusing on the main gravitational instability events that characterize the region (Section 2). Then, the modeling approach and the mechanical model are presented (Section 3). Results of the stress–strain analysis in dry conditions are first presented in Section 4 followed by the validation process, parametric and hydromechanical analyses. In Section 5 a general discussion is finally provided.

2. Study area

The study area is located in the Upper Valtellina region (Central Italian Alps), between the villages of Bormio and Santa Caterina Valfurva. The modeled region includes the right flank of the Frodolfo valley, where complex active gravitational processes are occurring (Fig. 1a).

The geological framework of the region, is related to the Austroalpine Nappe arrangement (Fig. 1b), which is composed by a crystalline basement of the pre-Permian age, with an N to E vergence. In the study area, the Campo Nappe with the Bormio Phyllites (metapelitic unit) outcrops (Fig. 1b; Ref. 45). This formation exhibits a pervasive schistosity with millimeter to centimeter spacing, defined by a submillimeter alternation of films of white mica, opaque minerals, and quartz-feldspathic microlithon, conferring a mylonitic texture to the rocks.[46] Rock masses are strongly deformed with isoclinal and minor transposed folds, recording a polyphase tectonic and metamorphic evolution during the Varisican and the Alpine orogeneses.[47–49] Locally, phyllites are characterized by the inclusion of magmatic bodies of late to

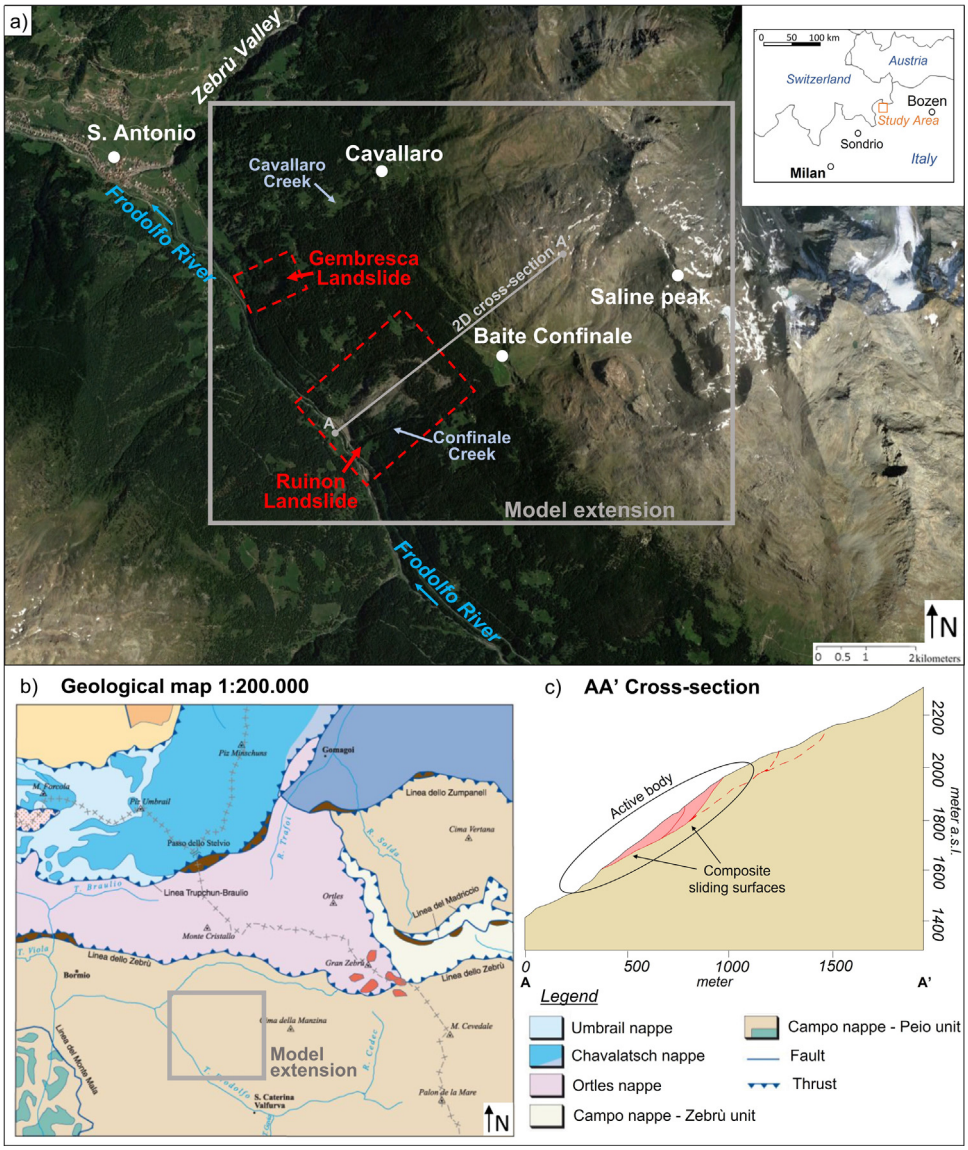

Fig. 1. (a) Satellite image of the study area[50]; active gravitational processes are highlighted in red while the modeled area is defined by the gray box. (b) Geological map of the area, in a 1:200.000 scale.[46] (c) Cross-section of the modeled slope along the Ruinon landslide body; the section tracing is defined in Fig. 1 A. (For interpretation of the references to color in this figure legend, the reader is referred to the web version of this article.)

post-Varisican and late Alpine age, and other bodies of the Campo Nappe unit as marbles and prasinites.[46]

Throughout its history, the valley has been affected by geomorphological dynamics, including fluvial and glacial processes, that have modeled its shape and caused the gradual mechanical stress release of the slopes.[51] As a result, the valley flanks are morphologically very steep slopes affected by gravitational phenomena, mainly controlled by climate dynamics.

The Ruinon landslide is located on the right flank of the valley and a few kilometers West of the Sant'Antonio village (Fig. 1a). This landslide is considered one of the most active cases in the Alpine region, with a main sliding surface located at approximately 70–90 m depth (Fig. 1c). With an estimated total volume of the sliding mass of 20 Mm^3.[52–55] This landslide has been showing an intense activity since 1981, with a major acceleration in 1987–1988 due to heavy rainfalls. Between the spring of 2014 and the fall of 2016, accelerated displacements were observed, and in June of 2019 landslide velocities increased to much higher values than ever before, reaching up to 1 m/day during approximately 5 months.[56] The main active body extends at elevations between 1600 and 2100 m.a.s.l., and is located at the base of a deep-seated gravitational slope deformation, which affects the entire slope up to its top at 3000 m.a.s.l..[51,52,57] Slope hazards related to the evolution of the landslide seriously impacted the regional road, located along the valley bottom.[56] Currently, the area affected by the landslide is monitored by both shallow and deep instrumentation, including three active piezometers, extensimeters, inclinometers, and a ground-based interferometric synthetic aperture radar (GBInSAR).

Other instability events involving smaller sliding mass volumes are present in the study area, mainly promoted by highly fractured rock masses. Among the main ones, on the right flank of the slope, there is the Gembresca landslide, which involves a sliding mass of approximately 10.000 m^3 and is currently in a dormant condition but can be reactivated by not particularly intense external forcings (Ref. 53; Fig. 1a). Ancient landslide deposits are also present along the valley bottom, suggesting an intense geomorphological activity of the slopes, even in earlier geological eras. Upstream of the Ruinon and Gembresca landslides, in a range between 1650 m.a.s.l. and 2830 m.a.s.l., rock scarps,

traction trenches, tensile fractures, and structural depressions valleys are present, approximately parallel to the main valley axis (predominantly in the WNW-ESE direction), indicating a strong gravitational activity of the slope.[51,52,57]

3. Methods

3.1. modeling approach

Numerical analysis of the Ruinon rock slope was performed using the open-source C++ MOOSE (Multiphysics Object-Oriented Simulation Environment) framework, with a FEM approach. MOOSE is a numerical framework developed, primarily, by Idaho National Laboratory.[58] It is a powerful tool for simulating multiphysics processes because of its nonlinear solver, that supports efficient coupling between systems of physical equations.

Multiple physical processes can be solved in an implicit, fully coupled way. MOOSE's project has generated a growing developer community of scientists and researchers actively involved in its continued development, and use in diverse research fields. Currently, MOOSE provides physics modules for solving problems in mechanics, porous flow, phase field modeling, and geochemical processes. All these modules are available to users, and any physics library can be included in the analyses.

The input file represents the core of the simulation, where separate components are used to define all the required elements. They include: the mesh geometry, the variables to solve for, the terms of the system of equations to be solved (called kernels), the boundary conditions, the initial conditions, and the calculation settings (solver options and timesteps). An external input mesh file, containing the geometric and topological information for MOOSE, can also be provided and called in the input file.

In this work, the geometrical model of the study area was built with Gmsh,[59] an external three-dimensional finite-element mesh generator (Fig. 2). In Gmsh, a model is defined using its boundary representation: a volume is bounded by a set of surfaces, a surface is bounded by a set of curves, and a curve is bounded by two endpoints. Each topological element can be uniquely named. By assigning a specific name to each surface, it is possible to apply a physical boundary condition for numerical analysis, simply by specifying the name of the surface in the MOOSE input file. The finite element mesh of the model is a tessellation of its geometry, with simple elements of various shapes (lines, triangles, quadrangles, tetrahedrons, prisms, hexahedrons, and pyramids), arranged in such a way that if two of them intersect, they do so only along one face, edge or node, and never otherwise.

The MOOSE simulator can output results in a variety of formats, from comma-separated plain text to common binary formats, that can be easily read with a popular post-processing software. In this work, output files of numerical simulations were read in a binary format with Paraview, an open-source multiple-platform for interactive visualization.[60]

3.2. Theoretical model

In this Section, the physical framework underlying the MOOSE implementation is discussed. In the model, a continuum representation of a homogeneous rock mass with a single fluid phase is considered. The following subsections describe the mechanical and hydrogeological processes represented in this formulation.

The mechanical model is based on the Tensor Mechanics module, a library of simulation tools that solve continuum problems. It can be used to simulate both small and finite strain constitutive frameworks, including elasticity, plasticity, creep, and damage due to cracking and property degradation. In this work, a finite strain formulation is used, and an elasto-plastic constitutive law is assumed.

The mechanical deformation is solved by the momentum balance under static assumption, leading to the evolution of effective stresses σ', defined as:

$$\frac{\vartheta \sigma'_{ij}}{\vartheta x_{ij}} + \rho_S g_i = 0$$

Where ρ_S is the density of the solid and g_i the gravity vector. The total strain rate, ε_{ij}, is decomposed into a reversible (elastic), ε^r_{ij}, and an irreversible (plastic), ε^i_{ij}, part:

$$\varepsilon_{ij} = \varepsilon^r_{ij} + \varepsilon^i_{ij}$$

The reversible part is assumed to follow a linear elastic relationship of the form:

$$\varepsilon^r_{ij} = C^e_{ijkl}\sigma'_{ij}$$

Where, $\sigma_{ij}{}'$ represents the effective stress tensor and C^e_{ijkl} is the elasticity tensor. The irreversible part of the strain rate follows a plastic law of the form:

$$\varepsilon^i_{ij} = \chi \frac{\partial g}{\partial \sigma_{ij}}$$

Where, g represents the plastic potential and χ is a scalar plastic multiplier. The specification of the yield criterion involved the Coulomb plastic formulation with a softening scheme, which postulated a linear relationship between shear strength on a plane and the normal stress acting on it:

$$\tau = c - \sigma_N tan\phi$$

where τ is the shear strength, σ_n is the normal stress (positive in tension), ϕ is in the angle of internal friction, and c is the cohesion. Combining the Coulomb criterion with the Mohr circle representation of stress state, and considering the admissible states, the Mohr–Coulomb (MC) failure criterion (f_s) in terms of principal stresses can be expressed as:

$$f_S = \frac{1}{2}(\sigma_1 - \sigma_3) + \frac{1}{2}(\sigma_1 + \sigma_3)\, sin\phi - c * cos\phi = 0$$

As many materials described by MC plasticity, such as rocks, cannot sustain large tensile stresses, a tensile cutoff in the failure criterion was also considered.[58] The yield surface representing the tension cutoff is defined as:

$$f_t = \sigma_3 - \sigma_t = 0$$

Where, σ_t is the tensile strength of the material. In 3 dimensions, MC plasticity is defined by six yielding functions that are planar in the coordinates of principal stresses. They produce a region of admissible stresses in the shape of a hexagonal pyramid. Adding the tensile cutoff, the pyramid's tip is removed, turning it into a triangular-based pyramid.

The plastic potential function is described by means of two functions: g_S and g_t, which are used to define the shear plastic flow and the tensile plastic flow, respectively. The function g_S corresponds to a, generally, non-associated law, and has the form:

$$g_S = \sigma_1 + \sigma_3 N_\omega$$

Where N_ω is a parameter that depends on the dilation angle, ω. This parameter should be less than or equal to the residual friction angle, which makes the flow rule non-associated or associated respectively; and

$$N_\omega = \frac{1 + sin\omega}{1 - sin\omega}$$

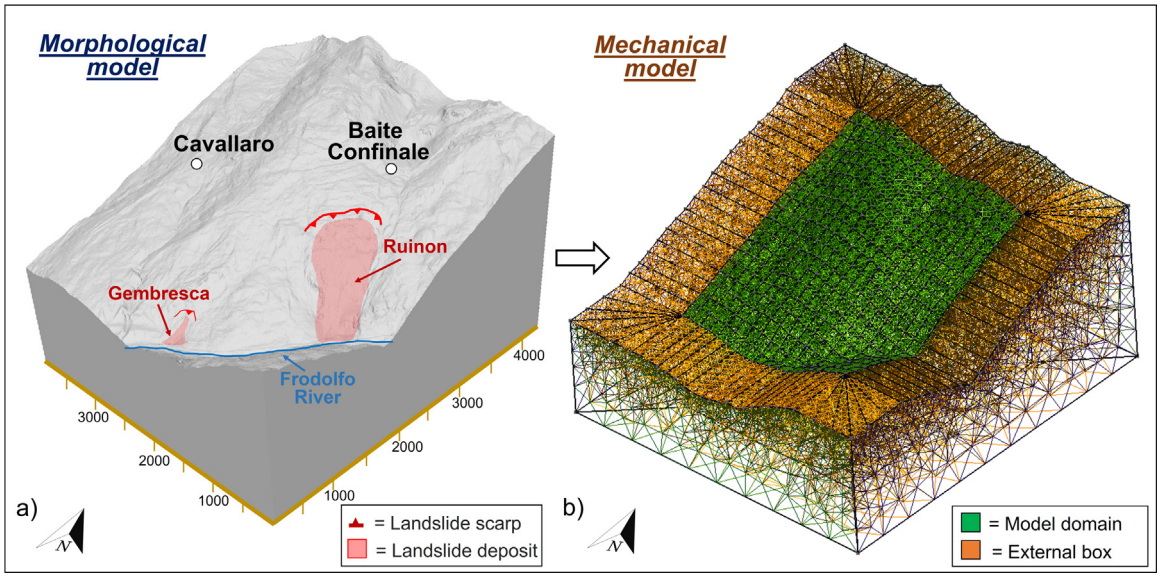

Fig. 2. (a) Main morphological features of the investigated area. (b) Implementation of the mechanical model from the slope morphological data.

The function g_t corresponds to an associated flow rule, and is written as:

$$g_t = f_t = \sigma_3 - \sigma_t$$

The mechanical framework presented above was also extended to account for pore fluid pressure and the evolution of porosity. MOOSE's PorousFlow module was used to compute pore pressure distribution in the model and couple it with the mechanical component. PorousFlow is a library of physics for fluid and heat flow, solving problems with an arbitrary number of phases (such as gas and liquid) and fluid components (species present in each fluid phase). The momentum balance equations for the fluid phase can be expressed as:

$$\beta \frac{\partial P_f}{\partial t} = \alpha_V \nabla^2 P_f - \varepsilon_V^{pl}$$

Where β is the compressibility factor, P_f is the pore pressure, α_V is the Biot coefficient (which is kept equal to 1 in the present work), and ε_V^{pl} the volumetric plastic strain. The pore pressure evolution is defined as:

$$P_f = P_h + \Delta P_f$$

Where, P_h is the hydrostatic pressure, and ΔP_f the excess pore pressure. Following Terzaghi's principle, the dependence of the pore fluid pressure, P_f, on the stress, σ_{ij}, is stated explicitly as:

$$\sigma_{ij} = \sigma_{ij}' - \alpha_V \delta_{ij} P_f$$

Where, σ_{ij}' is the effective stress (stresses are taken negative in compression). Volumetric strains control the evolution of porosity and the volume that can be occupied by a fluid. This process is fundamental to the coupling between fluid flow and solid mechanics. The total porosity, θ, is expressed as the sum of its initial value (θ_0) and the changed interconnected pore volume. In this model, the pore volume can be modified only by mechanical processes ($\Delta\theta_{mech}$). The evolution of the mechanical porosity contains two components, an elastic part:

$$\Delta\theta_{mech}^{e} = (1-\theta)\beta_S \Delta P_f$$

Where β_s is the compressibility coefficients of the solid, and a plastic part:

$$\Delta\theta_{mech}^{pl} = (1-\theta)\Delta\varepsilon_V^{pl}$$

being $\Delta\varepsilon_V^{pl}$ the increment of the volumetric plastic strain. Therefore, the total porosity is defined by the relation:

$$\theta = \theta_0 + \Delta\theta_{mech} = \theta_0 + \Delta\theta_{mech}^{e} + \Delta\theta_{mech}^{pl} = V_f/V$$

Where V_f is the volume occupied by the fluid. Considering the scale of the analysis (slope to regional), Darcy's law is used to relate the mass flux to the pore pressure gradient, under saturated conditions:

$$q = (v_f - v_s)\theta = -\frac{k}{\mu_f}(\nabla P_f - \rho_f g_i)$$

Where, v_f is the velocity of the fluid, v_s is the velocity of the solid, θ is the total porosity, μ_f is the viscosity of the fluid, k the permeability, and g_i the gravity vector. In the model, the permeability is considered isotropic and constant (i.e., not dependent on porosity).

3.3. Definition of the numerical model

The model domain develops along the North slope of the Valfurva valley (Fig. 1a). The modeled region lies between the Cavallaro valley to the North, and the Confinale valley to the South. To the West, the model limit is represented by the main valley floor with the Frodolfo River, flowing toward North-West, while to the East, the boundary is represented by the mountain ridge separating the Valfurva from the Zebrù valley. The model includes the areas where the main instability phenomena of the region have been observed, namely the Ruinon landslide and the Gembresca landslide.

The model has a squared shape base, and it covers an area of 15.8 km^2, calculated from the topographical surface. The highest elevation of the model is 3072 m.a.s.l., in correspondence with the Saline peak, and the lower one is 1370 m.a.s.l. along the main valley floor.

The geometrical model was developed based on the 2015 Digital Terrain Model of the Lombardy Region[61] and assuming a homogeneous and isotropic medium (Fig. 2a). The model was discretized into a finite-element mesh, by the definition of hexahedral zones (Fig. 2b). A maximum zone size of 200 meters was set, allowing the meshing software to create a grid that best fits the morphology, hence obtaining a significant reduction in computational time. To speed up computational times, the mesh

Table 1
Material parameters of the modeled slope obtained from laboratory tests and literature.[53]

Parameter	Value	Detection method
Density	2700 kg/m^3	Literature[53]
Young modulus	50 GPa	Laboratory test[53]
Poisson ratio	0.3	Laboratory test[53]
Cohesion	1 MPa	Laboratory test[53]
Friction angle	35°	Laboratory test[53]
Uniaxial compressive strength	80 MPa	Laboratory test[53]
Tensile strength	5 MPa	Laboratory test[53]
Porosity	0.1	Assumption based on literature data[53]

size increases with depth until it reaches maximum value of 500 m. To minimize the mechanical effects due to the presence of lateral geometric constraints in the modeled area, an 'outer box' was constructed by extending the lateral boundaries by 1000 m. Without this artifice, the application of Dirichlet-type mechanical boundary conditions at zero velocity (as is typically assumed in slope stability analyses), would result in the development of unrealistic stresses and strains near the boundaries. The excessive proximity of the boundaries to the area of interest would bring about significant computational errors. The definition of a rigid external box with computational continuity, allows to move the constriction zones away from the area of interest, while preserving the computational result.

Boundary conditions fixed at zero velocity were specified along the bottom boundary of the entire model, as well as at the external side boundaries.

As for the hydrogeological model, a basal water table was introduced, and free outer boundaries were defined by keeping pore pressures at constant values. The piezometric surface is represented by an external surface, introduced into the model by setting zero pore pressure along it. Then, hydrostatic pore pressures are calculated by the model, based on the location of the piezometric surface and gravity forces. In this study, the water table was built considering the presence of the Frodolfo river flowing at the base of the slope and taking into account the groundwater level measured in three piezometers located along the slope, in correspondence of the Ruinon landslide body. These represent fixed points through which the piezometric surface was built. The elaborated piezometric surface represents the shallowest aquifer, whose temporal evolution influences the mechanical evolution of the slope.

The model was parameterized according to laboratory tests conducted in previous studies[53] as summarized in Table 1. The mechanical parameters are derived from triaxial tests conducted on the core material of boreholes, drilled along the Ruinon landslide body. From the test results, the Hoek & Brown curvilinear fracture envelope[62] was defined, and the equivalent values of cohesion and friction angle, according to the MC criterion, were also defined. Considering the lithological homogeneity of the study area (Section 2), as a first approximation, the mechanical parameters derived were assumed to apply everywhere in the modeled domain. As discussed in Section 3.1, an elasto-plastic MC constitutive model was adopted for the main model domain, whereas a linear elastic behavior was assumed for the 'outer box'.

3.4. Numerical simulation

In a first step (Step 1), a static analysis was performed under dry conditions, considering the mechanical parameters presented in Table 1. The model was then validated, by comparing simulation results with geomorphological observations, i.e., by overlaying satellite images with model results (see Section 4). Four different meshes were used as inputs to evaluate the influence of the grid size on numerical results (stress and strain distribution), and to identify the best configuration, in terms of computational cost and accuracy of the results.

Once the model was validated and the best performing mesh was identified, the next two steps (Step 2 and 3) included a mechanical and a hydromechanical parametric analysis, respectively. In Step 2, the cohesion value was varied from 1 MPa to 0.25 MPa, to evaluate and quantify the effect of strength parameters in the development of irreversible strains. In Step 3, three different piezometric level scenarios were defined, based on the field data (piezometers) installed along the Ruinon slope. The water level scenarios were defined as follows: (i) ordinary regime (water level in the piezometer at 40 meters depth), (ii) maximum regime (30 meters depth), and (iii) an extreme regime (20 meters depth). The aim of this parametric study was to analyze the role of pore pressure in the development of irreversible strains. The evolution of effective stresses at varying groundwater level was also explored, and was used in the thermo-hydro-mechanical analysis presented in the 'Part 2' companion paper.[44]

4. Results

Considering the purpose of this study, model results were analyzed in terms of the development of irreversible deformations along the slope, as well as the redistribution of the stress–strain field within the model domain. With reference to the theoretical background presented in Section 3.2, plastic deformation defines the irreversible part of the strain tensor, highlighting areas where gravitational instabilities preferentially develop. The magnitude and distribution of shear plastic strains are analyzed below.

Introducing the elasto-plastic mechanical properties detected with laboratory tests and shown in Table 1 (Step 1, discussed in Section 3.3), it was possible to simulate the stress–strain state along the model domain, brought about by gravity and 3D topographical constraints (Fig. 3a–c).

It can be observed that zones of high deformation develop in the eastern portion of the model and on its southern border. Focusing on the magnitude and distribution of shear plastic strain, two main clusters of large deformation were identified. The first one, corresponding to the Confinale valley, extends from the bottom of the Frodolfo valley up to an elevation of 2000 m.a.s.l..

The maximum shear plastic strain values detected lie in the range between 0.03 and 0.04%. The second cluster of large deformation is located along the principal Frodolfo valley, with a main concentration of strains on the southern limit of the model (Fig. 3b).

To validate the model and relate simulation outputs to the gravitational processes that affect the study area, a comparison between model outputs and geomorphological observations was performed. Hence, the satellite image of the study area[50] was overlaid to the model domain, by matching each pixel of the image to the model coordinates. As shown in Fig. 2d, a good correlation was observed between the location of the simulated irreversible deformation zones and the gravitational instability events, affecting the modeled area (Ruinon and Gembresca landslide). Moreover, analyzing the 2D cross sections taken along the model domain (Fig. 3), the geometries of the landslide bodies (Fig. 1c) were reproduced with a good qualitative accuracy. Cross-Section A in Fig. 3e explores the evolution of the Gembresca landslide, which has been documented to involve only a shallow and limited portion of the slope,[53] as correctly simulated by the model. Concerning the Ruinon landslide, geomorphological and geomechanical observations carried out by previous authors[52,53,55] highlighted a composite slip surface at about 80 m depth, and an upper scarp of the landslide body at about 2100 m

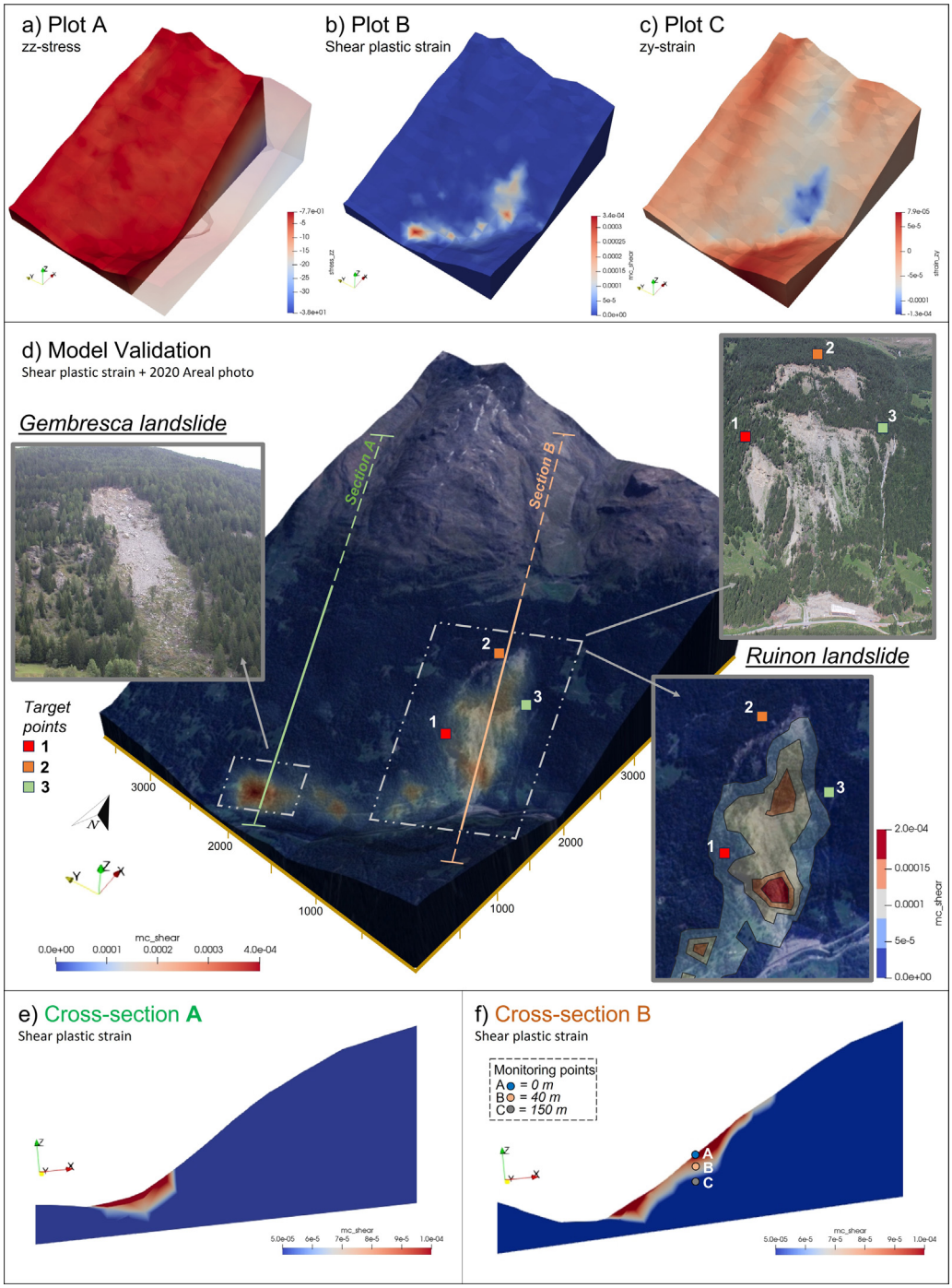

Fig. 3. (a–c) Results of the stress–strain analysis in dry conditions. (d) Model validation by overlying shear plastic strains with satellite images of the study area.[50] (e–f) Section of the model representing plastic shear deformation along the landslide bodies.

a.s.l (Fig. 1). The cross-section B of Fig. 3f, cuts the slope along the Ruinon landslide body, following its sliding direction. In this cross-section, it can be observed that the maximum irreversible deformations are simulated in the shallowest portion of the slope and become zero at a depth greater than 150 m. Considering these observations, in both 2D and 3D space, the model adequately simulates the gravitational evolution of the slope, and the observed volumes of the sliding masses are comparable with the simulation results. After model validation, different mesh sizes were tested to identify the best configuration, in terms of computational cost and accuracy of results. Mesh sizes of 100, 150, 200, and 250 meters were tested (Fig. 4).

It may be observed that the distribution of plastic strains is consistent in all mesh configurations (Fig. 4), where the two main clusters of irreversible deformation discussed earlier during the validation process are maintained. However, with a finer mesh, the geometries of the landslide bodies are better defined. In addition, adopting mesh sizes of 100 or 150 m the presence of deformation along the valley bottom is well reproduced. With a mesh size of 100 m, the model simulation ends after 1000 s using a standard desktop multicore workstation. By increasing the mesh size, the computation time is significantly reduced, while the limits of high deformation bodies become less defined. The mesh size of 250 m is not sufficient to simulate the gravitational

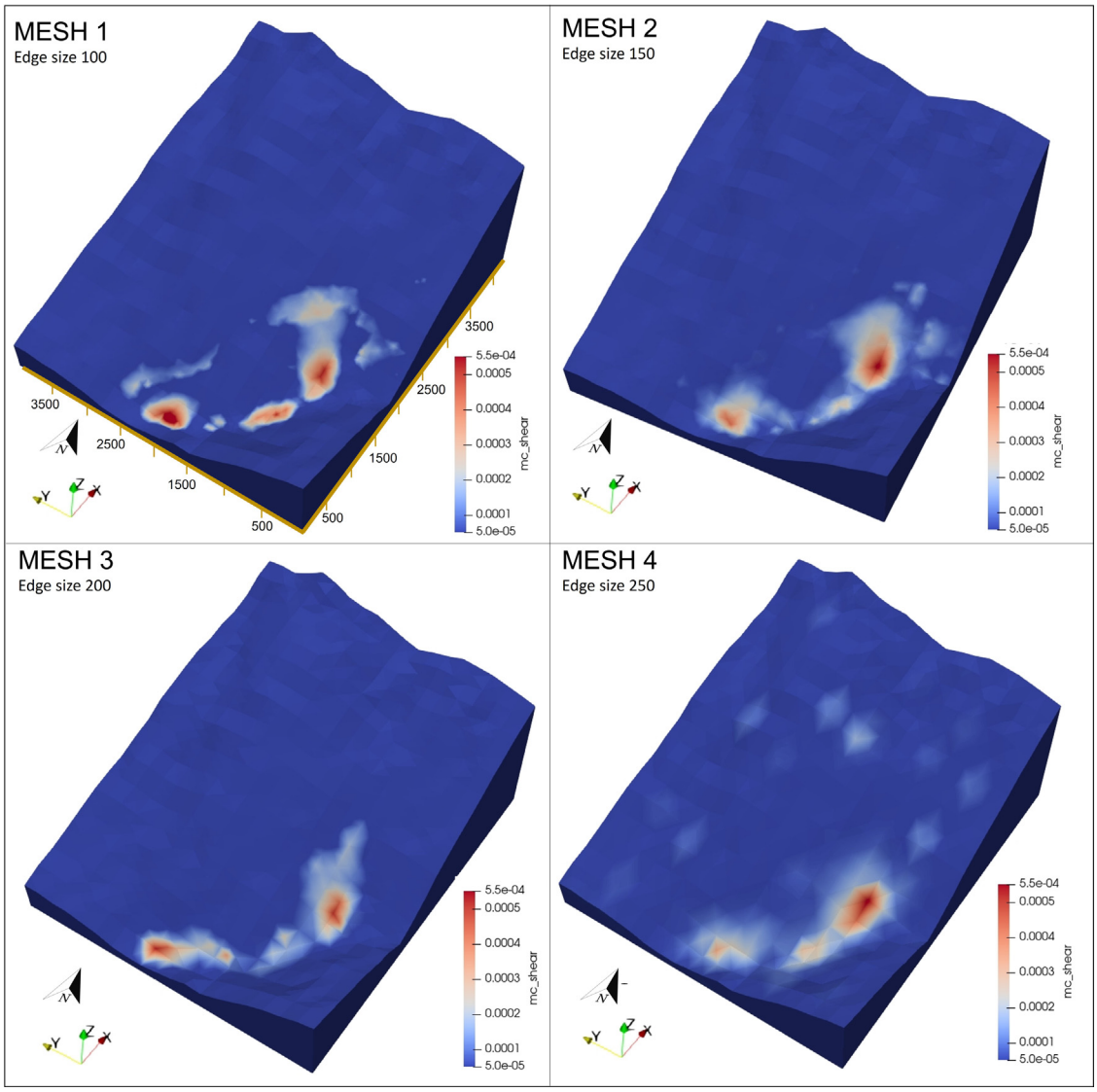

Fig. 4. Distribution of plastic shear strains resulted by considering different computational mesh sizes.

instabilities affecting the model domain, exhibiting a very poor definition due to the large grid size. Computation times are reduced to 20 s for the 200 m mesh, and to 15 s for the 250 m mesh. Considering the good consistency of the outputs held by the models with different mesh sizes, it was deemed appropriate to continue the analysis with the 200 m grid, on which the validation process was performed. In this way, computational times could be kept low, even considering the subsequent introduction of the hydro-mechanical coupling, likely to lead to a substantial increase in simulation time.

Further, a parametric analysis was performed (Step 2), to explore the relation between cohesion values and the development of plastic strains (Fig. 5). Decreasing cohesion from 1 MPa to 0.25 MPa, led to a considerable increase in the development of plastic deformation. However, it can be observed that even if shear plastic strains increase in magnitude, neither the extent of areas affected by irreversible deformation, nor the location of the two clusters of high strains identified during the model validation step (Fig. 4), change significantly. To analyze the trend in strain magnitude with the evolution of mechanical parameters, a vertical profile was defined, in correspondence of the Ruinon landslide body and three reference points A, B, C (see Fig. 3) were monitored: Point "A" is located on the slope surface, Point "B" inside the landslide body (40 meters depth), and Point "C" at a depth of 150 meters (i.e. below the slip surface detected by geotechnical site investigations). As shown in Fig. 5e, a logarithmic relationship could be identified between cohesion values and normalized shear strain magnitude values (defined as the ratio of the measured value to the maximum simulated one) at all the three monitoring points (A, B, and C): starting from low strain values (0.001 to 0.003%) at 1 MPa of cohesion (quite stable conditions of the slope), large strain values (0.05 to 0.06%) were obtained at a cohesion of 0.25 MPa.

The two most shallow points A and B (orange and blue lines in Fig. 5e) exhibited a similar behavior with curves that follow the same evolutionary trend. On the other hand, the deeper point at 150 m depth (gray line in Fig. 5e) showed a more stable behavior, even at very low cohesion values (0.25 to 0.5 MPa). This trend is consistent with the geomechanical evolution of the slope reconstructed from site investigations, suggesting the slope to be stable at depths greater than 100 meters (below the sliding surface, located at 70–90 m depth). In Step 3 of numerical modeling, hydrogeological factors were introduced, considering the three different water level scenarios defined in Section 3.3. A clear correlation was shown between the piezometric surface level and the evolution of plastic deformation, with effects

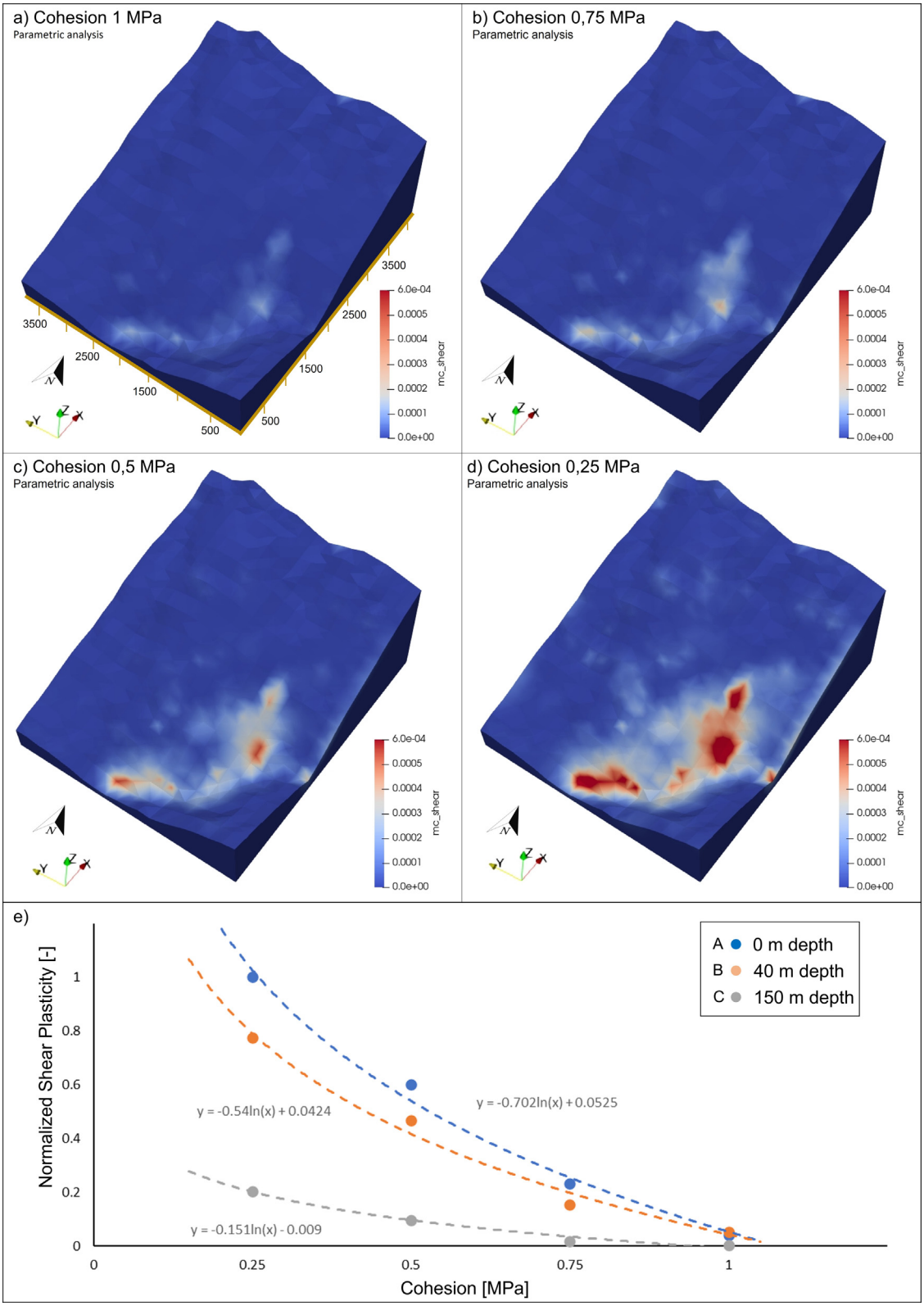

Fig. 5. (a–d) Distribution of plastic shear strains obtained from parametric analysis by introducing different values of mechanical parameters. (e) Evolution of plastic strain values (y-axis) as cohesion decreases (x-axis); a logarithmic equation is written for each case near the corresponding curve.

comparable to those induced by the mechanical degradation process (Fig. 6). Furthermore, a linear dependence between effective shear stresses and pore pressure was observed (i.e., at constant depth, as pore pressures increase, the effective shear stresses decay, according to a linear relationship).

Comparing the "dry-model" with the "scenario-I drained-model" (Section 3.3) results, an increase in strain values was observed. As the piezometric level increases, the magnitude of plastic deformation increases, while the areal distribution of

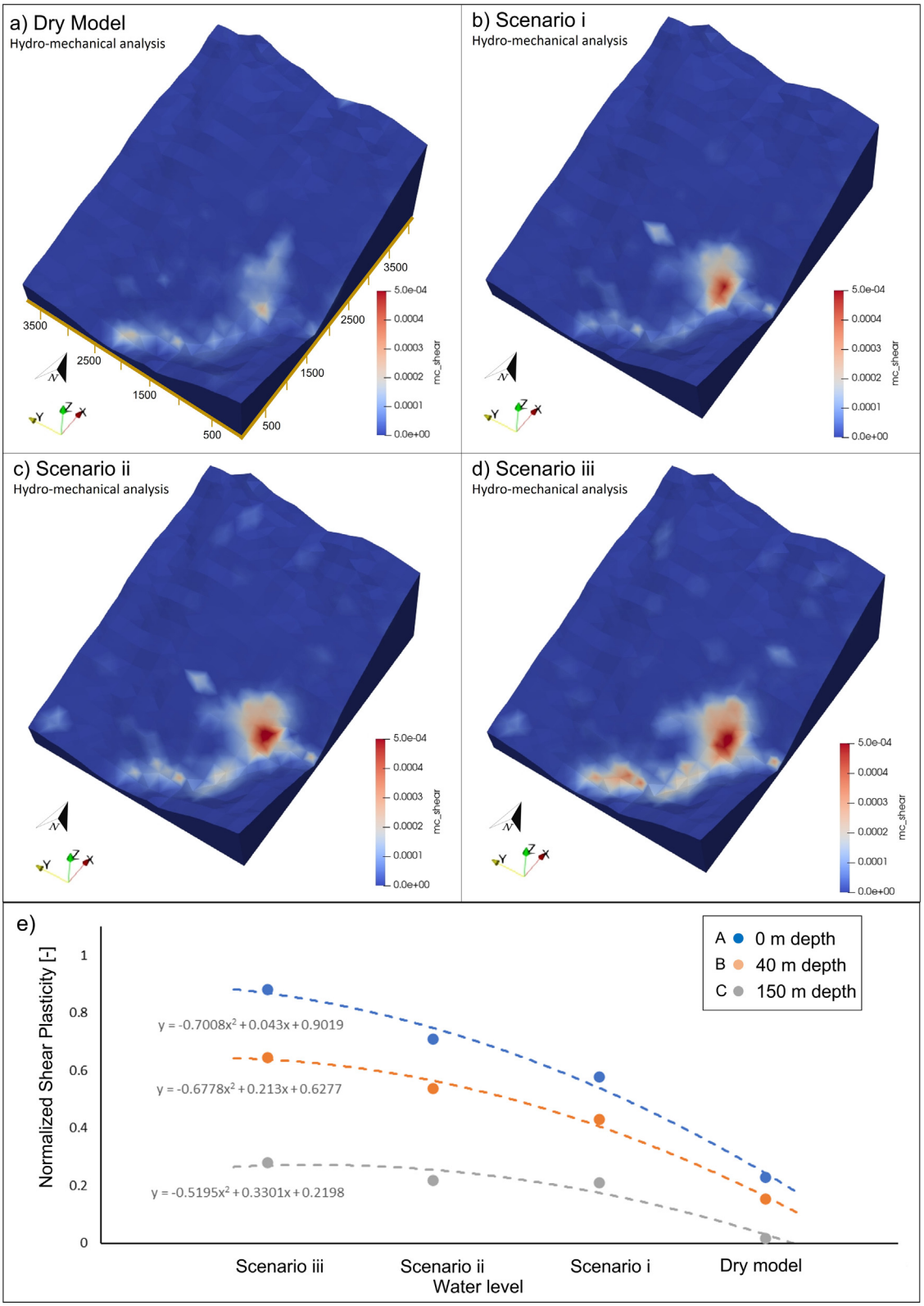

Fig. 6. (a-d) Distribution of plastic shear strains obtained from hydromechanical analysis by introducing different scenarios of groundwater level. (e) Evolution of plastic strain values (y axis) at different ground water level scenarios (x axis); a polynomial relation is highlighted.

zones under irreversible deformation remains the same. However, the rising water level also induces the development of plastic strains along the main valley floor, as a result of the increase in pore pressures at the bottom of both valley flanks. Analyzing the monitoring points A, B, C along the Ruinon landslide body (Fig. 3), a polynomial (parabolic) relation was detected between the magnitude of plastic shear strains and the simulated trend of the piezometric level (Fig. 6e). The introduction of pore pressures (transition between dry model and "scenario-I drained-model") generates a sudden increase in strain values (as an example, the normalized strain values recorded at point A in Fig. 6 increased from 0.3 to 0.7), while the subsequent progressive rising of the water table causes only a limited strain growth (at the same point, normalized strain values increased from 0.7 to 0.9). In general, it can be observed that the effects of mechanical degradation and changes in pore pressure are similar. However, decreasing the cohesion has a greater influence on strain rates than increasing the pore pressure. Overall, a good correspondence with the observed geotechnical evolution of the slope is also maintained in the hydro-mechanical analysis, with higher plastic strain (normalized values between 0.5 and 0.9, Fig. 6e) in correspondence of the shallower points and greater stability (normalized values between 0.2 and 0.5, Fig. 6e) at the deepest one.

5. Discussion and conclusions

Analysis and understanding of slope instability processes is crucial for landslide forecasting, risk mitigation, and infrastructure protection efforts.[63,64] To account for the physical process of landslide initiation and simulate slope stress–strain evolution under different external loads, numerical methods are widely employed. In this work, a numerical 3D FEM model was developed for an Alpine slope, exhibiting gravitational instability. The main goal of this work was to assess landslide-prone areas within a large domain by analyzing the physical processes behind the slope instability initiation. The model employed in this study assumes a homogeneous and isotropic material, and no slip surfaces were established *a priori*. From morphological data and laboratory test results, a simple mechanical model was defined using a standard elasto-plastic constitutive law. In a first step of the analysis, a static simulation was performed under dry conditions. Then, mechanical and hydromechanical parametric analyses were performed, exploring different mechanical and hydrogeological scenarios. Numerical results are shown to accurately reproduce the extent of the areas that are most prone to gravitational instabilities: overlapping satellite images with the model outputs, a good correspondence between areas of simulated irreversible deformation, and the location of gravitational instability phenomena was verified.

Then, two parametric analyses allowed us to explore different stress–strain evolution scenarios. In both cases, a clear correlation between input factors and the magnitude of strain has been shown, while the spatial distribution of irreversible deformations does not significantly change.

The main advantage of this approach is the ability to simulate gravitational instability processes without needing a large amount of input data. The crucial input information is the topographical surface, the mechanical strength parameters (such as cohesion and friction angle) and the depth of the groundwater table. Concerning mechanical data, it has been demonstrated that decreasing values of cohesion (from 1 to 0.25 MPa) result in an increase in the magnitude of strains (0.001 to 0.06%), without a significant change in the distribution of unstable zones. Therefore for other case studies, in the absence of measured data, representative mechanical values estimated from the literature may be sufficient to identify the areas most prone to instability. Then, different scenarios of mechanical evolution can be easily accounted for, through a parametric analysis. The same concept can be also applied to the pore pressure distribution, since it has been shown that the mean depth of the water table is sufficient to identify most active areas. Also, for the latter factor, different scenarios of pore pressure evolution can be easily explored through a hydromechanical analysis.

The possibility of accounting for the evolution over time of driving factors, such as morphology, mechanical parameters, and climate-related variables, among others, and the inclusion of a 3D topography is an advantage over statistical and LE-based methods. Because of its physically based structure, with this model it is possible to dynamically incorporate the evolution of landslide controlling factors over time, and assess the potential development of high landslide susceptibility zones.

Moreover, the results of this work show that numerical methods can be a potentially powerful tool to analyze slopes' evolution, even when in situ and satellite areal monitoring data are not available. In fact, in some regions, the analysis of satellite data is very difficult, due to the unfavorable orientation of the slopes with respect to the satellite orbits, or to the presence of very steep valley flanks covered by vegetation. In these cases, slope deformation data over time are not available. A physics-based approach, such as the one presented in this paper, can overcome this problem by identifying active zones and evaluating slope evolution scenarios, representing a valuable support tool for landslide risk forecasting and mitigation. In addition, this method can be useful in defining the priority and the design of landslide monitoring systems, since it allows the detection of the areas most prone to gravitational instabilities, where planning efforts need to be focused. This applies not only to current slope conditions, but also to different (future) mechanical or hydrological scenarios, allowing monitoring actions to be planned over time.

In this work, a homogeneous and isotropic model was adopted that does not include lithologic variations or the presence of significant geologic features such as faults or thrusts. This assumption is considered valid as the simulated domain is lithologically homogeneous (Fig. 1b, Section 2), but it may constitute an oversimplification for other case studies. Numerical stress–strain models still find applicability, even in complex geologic settings,[42] leading, however, to much higher computational costs, especially for large modeled regions, thus making it unsuitable for practitioners' calculations. In some cases, with high complexity (being typical in Alpine environments), this may represent a limitation and the method may find little applicability. One solution may be represented by the ability to perform different parametric analyses, allowing the exploration of the presence of various geologic features, by simply varying the mechanical properties set on the different units of the model domain.

Focusing on the Ruinon landslide body, in addition to correctly identifying the unstable area, the presented analysis allowed us to calculate the stress state along its sliding surface: the basal mean shear stresses detected at a depth of about 80 m varies between 0.1 and 0.5 MPa, depending on the groundwater level. These values will be used as input factors in the development of a 1D thermo-hydro-mechanical model of the landslide, that will allow us to simulate the behavior and the evolution of the Ruinon landslide through a physics-based approach (see 'Part 2' companion paper[44]). A linear dependency between the pore pressure and the effective shear stresses has been also detected with the FEM analysis (Section 4). This will allow, as a first approximation, to use a simple linear equation to calculate the stress state along the slip surface of the landslide, depending only on the depth of the water table.

Therefore, this work represents a first step toward the definition of a multi-approach analysis, in which different methods

converge toward the definition of a physics-based criterion, that allows the evaluation of landslide scenarios, starting from their geometric and stress–strain assessment (FEM analysis, discussed in this work), toward the simulation of their velocities and their stability over time (1D THM mathematical modeling[44]).

CRediT authorship contribution statement

Andrea Morcioni: Conceptualization, Methodology, Data curation, Software, Formal analysis, Writing – original draft. **Tiziana Apuani:** Visualization, Data curation, Supervision, Writing – review & editing. **Francesco Cecinato:** Visualization, Data curation, Supervision, Writing – review & editing. **Manolis Veveakis:** Methodology, Validation, Visualization, Supervision, Writing – review & editing.

Declaration of competing interest

The authors declare that they have no known competing financial interests or personal relationships that could have appeared to influence the work reported in this paper.

Data availability

Data will be made available on request.

Acknowledgments

This research has been carried out in the framework of the Doctoral Program in Earth Sciences of the University of Milan and supported by the NSF CMMI-2042325 award. The Authors are also grateful to ARPA Lombardia for making the field monitoring data available.

References

1. Crozier MJ. Geomorphology deciphering the effect of climate change on landslide activity: A review. *Geomorphology*. 2010;124(3-4):260–267. http://dx.doi.org/10.1016/j.geomorph.2010.04.009.
2. Stoffel M, Tiranti D, Huggel C. Science of the total environment climate change impacts on mass movements — Case studies from the European Alps. *Sci Total Environ*. 2014;493:1255–1266. http://dx.doi.org/10.1016/j.scitotenv.2014.02.102.
3. Scavia C, Barbero M, Castelli M, et al *Evaluating Rockfall Risk : Some Critical Aspects*. Published online; 2020:1–29. http://dx.doi.org/10.3390/geosciences10030098.
4. Jomelli V. Impacts of future climatic change (2070–2099) on the potential occurrence of debris flows : A case study in the Massif des Ecrins. 2009 http://dx.doi.org/10.1007/s10584-009-9616-0, (November).
5. Stoffel M, Huggel C. Effects of climate change on mass movements in mountain environments. *Prog Phys Geogr*. 2012;36(3):421–439. http://dx.doi.org/10.1177/0309133312441010.
6. Shan W, Hu Z, Guo Y, et al The impact of climate change on landslides in southeastern of high-latitude permafrost regions of China, 3 (february). 2015:1–11. http://dx.doi.org/10.3389/feart.2015.00007.
7. Gariano SL, Guzzetti F. Landslides in a changing climate. *Earth-Sci Rev*. 2016;162:227–252. http://dx.doi.org/10.1016/j.earscirev.2016.08.011.
8. Guzzetti F, Carrara A, Cardinali M, Reichenbach P. Landslide hazard evaluation: A review of current techniques and their application in a multi-scale study, Central Italy. *Geomorphology*. 1999;31:181–216. http://dx.doi.org/10.1016/S0169-555X(99)00078-1.
9. Guzzetti F, Reichenbach P, Ardizzone F, Cardinali M, Galli M. Estimating the quality of landslide susceptibility models. *Geomorphology*. 2006;81(1):166–184. http://dx.doi.org/10.1016/j.geomorph.2006.04.007.
10. Carrara A, Guzzetti F, Cardinali M, Reichenbach P. Use of GIS technology in the prediction and monitoring of landslide hazard. *Natural Hazards*. 1999;20:117–135. http://dx.doi.org/10.1023/a:1008097111310.
11. Reichenbach P, Rossi M, Malamud BD, Mihir M, Guzzetti F. A review of statistically-based landslide susceptibility models. *Earth-Sci Rev*. 2018;180:60–91. http://dx.doi.org/10.1016/j.earscirev.2018.03.001.
12. Aleotti P, Chowdhury R. Landslide hazard assessment: Summary review and new perspectives. *Bull Eng Geol Environ*. 1999;58(1):21–44. http://dx.doi.org/10.1007/s100640050066.
13. Borga M, Dalla Fontana G, Da Ros D, Marchi L. Shallow landslide hazard assessment using a physically based model and digital elevation data. *Environ Geol*. 1998;35(2):81–88. http://dx.doi.org/10.1007/s002540050295.
14. Burton A, Bathurst JC. Physically based modelling of shallow landslide sediment yield at a catchment scale. *Environ Geol*. 1998;35(2):89–99. http://dx.doi.org/10.1007/s002540050296.
15. Godt JW, Baum RL, Savage WZ, Salciarini D, Schulz WH, Harp EL. Transient deterministic shallow landslide modeling: Requirements for susceptibility and hazard assessments in a GIS framework. *Eng Geol*. 2008;102(3):214–226. http://dx.doi.org/10.1016/j.enggeo.2008.03.019.
16. Gischig V, Amann F, Moore JR, Loew S, Eisenbeiss H, Stempfhuber W. Composite rock slope kinematics at the current randa instability, Switzerland, based on remote sensing and numerical modeling. *Eng Geol*. 2011;118(1–2):37–53.
17. Brideau M-A, Pedrazzini A, Stead D, Froese C, Jaboyedoff M, Zeyl Dvan. Three-dimensional slope stability analysis of south peak, crowsnest pass, alberta, Canada. *Landslides*. 2011;8(2):139–158. http://dx.doi.org/10.1007/s10346-010-0242-8.
18. Wang S, Ni P. Application of block theory modeling on spatial block topological identification to rock slope stability analysis. *Int J Comput Methods*. 2014;11(1). http://dx.doi.org/10.1142/S0219876213500448.
19. Griffiths DV, Lane PA. Slope stability analysis by finite elements. *Géotechnique*. 1999;49(3):387–403. http://dx.doi.org/10.1680/geot.1999.49.3.387.
20. Cheng YM, Lansivaara T, Wei WB. Two-dimensional slope stability analysis by limit equilibrium and strength reduction methods. *Comput Geotech*. 2007;34(3):137–150. http://dx.doi.org/10.1016/j.compgeo.2006.10.011.
21. Camera CAS, Bajni G, Corno I, Raffa M, Stevenazzi S, Apuani T. Introducing intense rainfall and snowmelt variables to implement a process-related non-stationary shallow landslide susceptibility analysis. *Sci Total Environ*. 2021;786:147360. http://dx.doi.org/10.1016/j.scitotenv.2021.147360.
22. Bajni G, Camera CAS, Apuani T. Deciphering meteorological influencing factors for Alpine rockfalls: A case study in Aosta valley. *Landslides*. 2021;18(10):3279–3298. http://dx.doi.org/10.1007/s10346-021-01697-3.
23. Bajni G, Camera CAS, Brenning A, Apuani T. Assessing the utility of regionalized rock-mass geomechanical properties in rockfall susceptibility modelling in an Alpine environment. *Geomorphology*. 2022;415:108401. http://dx.doi.org/10.1016/j.geomorph.2022.108401.
24. Loche M, Scaringi G, Yunus AP, et al Surface temperature controls the pattern of post-earthquake landslide activity. *Sci Rep*. 2022;12(1):988. http://dx.doi.org/10.1038/s41598-022-04992-8.
25. Lateltin O, Haemmig C, Raetzo H, Bonnard C. Landslide risk management in Switzerland. *Landslides*. 2005;2(4):313–320. http://dx.doi.org/10.1007/s10346-005-0018-8.
26. Beniston M, Farinotti D, Stoffel M, et al The European mountain cryosphere: A review of its current state, trends, and future challenges. *Cryosphere*. 2018;12(2):759–794. http://dx.doi.org/10.5194/tc-12-759-2018.
27. Shou KJ, Lin JF. Evaluation of the extreme rainfall predictions and their impact on landslide susceptibility in a sub-catchment scale. *Eng Geol*. 2020;265(2019):105434. http://dx.doi.org/10.1016/j.enggeo.2019.105434.
28. Thiebes B, Bell R, Glade T, Jäger S, Anderson M, Holcombe L. A webgis decision-support system for slope stability based on limit-equilibrium modelling. *Eng Geol*. 2013;158:109–118. http://dx.doi.org/10.1016/j.enggeo.2013.03.004.
29. Thiebes B, Bell R, Glade T, et al Integration of a limit-equilibrium model into a landslide early warning system. *Landslides*. 2014;11(5):859–875. http://dx.doi.org/10.1007/s10346-013-0416-2.
30. Gu T, Wang J, Fu X, Liu Y. GIS and limit equilibrium in the assessment of regional slope stability and mapping of landslide susceptibility. *Bull Eng Geol Environ*. 2015;74(4):1105–1115. http://dx.doi.org/10.1007/s10064-014-0689-2.
31. Camera C, Apuani T, Masetti M. Modeling the stability of terraced slopes: An approach from Valtellina (Northern Italy). *Environ Earth Sci*. 2015;74(1):855–868. http://dx.doi.org/10.1007/s12665-015-4089-0.
32. Bishop AW. The use of the slip circle in the stability analysis of slopes. *Géotechnique*. 1955;5(1):7–17. http://dx.doi.org/10.1680/geot.1955.5.1.7.
33. Morgenstern NR, Price VE. The analysis of the stability of general slip surfaces. *Géotechnique*. 1965;15(1):79–93. http://dx.doi.org/10.1680/geot.1965.15.1.79.
34. Janbu N. *Slope Stability Computations*. Publ Wiley Sons, Inc. Published online; 1973.
35. Firincioglu BS, Ercanoglu M. Insights and perspectives into the limit equilibrium method from 2D and 3D analyses. *Eng Geol*. 2021;281(2019):105968. http://dx.doi.org/10.1016/j.enggeo.2020.105968.
36. Liu SY, Shao LT, Li HJ. Slope stability analysis using the limit equilibrium method and two finite element methods. *Comput Geotech*. 2015;63:291–298. http://dx.doi.org/10.1016/j.compgeo.2014.10.008.
37. Rawat S, Gupta AK. Analysis of a nailed soil slope using limit equilibrium and finite element methods. *Int J Geosynth Gr Eng*. 2016;2(4):1–23. http://dx.doi.org/10.1007/s40891-016-0076-0.
38. Ureel S, Momayez M. An investigation of the limit equilibrium method and numerical modeling for rock slope stability analysis. In: *Rock Mechanics*

and Its Applications in Civil, Mining, and Petroleum Engineering. 218–227. http://dx.doi.org/10.1061/9780784413395.025.
39. Donald IB, Giam SK. Application of the nodal displacement method to slope stability analysis. In: *Fifth Australia-New Zealand Conference on Geomechanics: Prediction Versus Performance; Preprints of Papers: Prediction Versus Performance; Preprints of Papers*. 1988:456–460.
40. Wei WB, Cheng YM, Li L. Three-dimensional slope failure analysis by the strength reduction and limit equilibrium methods. *Comput Geotech*. 2009;36(1–2):70–80. http://dx.doi.org/10.1016/j.compgeo.2008.03.003.
41. Tschuchnigg F, Schweiger HF, Sloan SW, Lyamin AV, Raissakis I. Comparison of finite-element limit analysis and strength reduction techniques. *Géotechnique*. 2015;65(4):249–257. http://dx.doi.org/10.1680/geot.14.P.022.
42. Morcioni A, Apuani T, Cecinato F. Piuro landslide: 3D hydromechanical numerical modelling of the 1618 event. *Geosci*. 2023;13(2). http://dx.doi.org/10.3390/geosciences13020049.
43. Wolter A, Havaej M, Zorzi L, et al Exploration of the kinematics of the 1963 vajont slide, Italy, using a numerical modelling toolbox. *J Eng Geol Environ*. 1963;2013(TOPIC 6):599–612. http://dx.doi.org/10.4408/IJEGE.2013-06.B-58.
44. Morcioni A, Apuani T, Cecinato F, Veveakis M. Landslide susceptibility evaluation in Alpine environment: 2, thermo-hydro-mechanical modeling for the response to climate-related variables. *Geomech energy Environ*. 2023. http://dx.doi.org/10.1016/j.gete.2023.100494.
45. Bonsignore G, Borgo A, Gelati R, et al *Note Illustrative Della Carta Geologica D'Italia, Foglio 8—Bormio*. Roma: Serv Geol d'Italia; 1969 Published online.
46. Montrasio A, Berra F, Cariboni M, et al *Note Illustrative Della Carta Geologica D'Italia Alla Scala 1:50.000 - Foglio Bormio*. Istituto Superiore per la Protezione e la Ricerca Ambientale Servizio Geologico d'Italia Organo cartografico dello Stato; 1990 Published online.
47. Conti P. MANATscHAL Ganre, Pfister M. Synrift sedimentation, Jurassic and Alpine tectonics in the central Ortler nappe (Eastern Alps, Italy). *Eclogae Geol Helv*. 1994;87(1):63–90.
48. Froitzneim N, Manatschal G. Kinematics of Jurassic rifting, mantle exhumation, and passive-margin formation in the Austroalpine and Penninic nappes (eastern Switzerland). *Bull Geol Soc Am*. 1996;108(9):1120–1133. http://dx.doi.org/10.1130/0016-7606(1996)108.
49. Gregnanin A, Valle M. Deformation and metamorphism in the Austroalpine Oetztal-Stubai Complex (Part II); Early-Alpine evolution in basement and cover. *Ital J Geosci*. 1995;114(2):393–409.
50. Google E. Google Earth. doi:earth.google.com/web/.
51. Agliardi F, Crosta G, Zanchi A. Structural constraints on deep-seated slope deformation kinematics. *Eng Geol*. 2001;59(1-2):83–102. http://dx.doi.org/10.1016/S0013-7952(00)00066-1.
52. Crosta GB, Agliardi F. Failure forecast for large rock slides by surface displacement measurements. *Can Geotech J*. 2003;40(1):176–191. http://dx.doi.org/10.1139/t02-085.
53. Griffini L. *Valutazione Delle Condizioni Di Stabilità Della Frana Del Ruinon E Aree Limitrofe*. Published online; 2004.
54. Del Ventisette C, Casagli N, Fortuny-Guasch J, Tarchi D. Ruinon landslide (Valfurva, Italy) activity in relation to rainfall by means of GBInSAR monitoring. *Landslides*. 2012;9(4):497–509. http://dx.doi.org/10.1007/s10346-011-0307-3.
55. Crosta GB, Agliardi F, Rivolta C, Alberti S, Dei Cas L. Long-term evolution and early warning strategies for complex rockslides by real-time monitoring. *Landslides*. 2017;14(5):1615–1632. http://dx.doi.org/10.1007/s10346-017-0817-8.
56. Carlà T, Gigli G, Lombardi L, Nocentini M, Casagli N. Monitoring and analysis of the exceptional displacements affecting debris at the top of a highly disaggregated rockslide. *Eng Geol*. 2021:294. http://dx.doi.org/10.1016/j.enggeo.2021.106345.
57. Crosta G, Zanchi A. Deep seated slope deformations: Huge, extraordinary, enigmatic phenomena. 2000:351–358. http://dx.doi.org/10.1680/lirtapv1.34617.0058,
58. Icenhour C, Keniley S, Permann C, Lindsay A, Martineau R, Curreli D. *Multi-Physics Object Oriented Simulation Environment (MOOSE)*. Idaho Natl Lab.; 2018 (November).
59. Geuzaine C, Remacle J-F. *Gmsh Reference Manual*. Published online; 2023 https://gmsh.info/dev/doc/texinfo/gmsh.pdf.
60. Ayachit U, Geveci B, Quammen C, et al *ParaView: User Guide*. Kitware Inc. Published online; 2018:274. http://paraview.orghttp//kitware.com.
61. Regione Lombardia. *DTM 5X5 - Modello Digitale Del Terreno*. Published online; 2015.
62. Eberhardt E. The Hoek-Brown failure criterion. *Rock Mech Rock Eng*. 2012;45(6):981–988. http://dx.doi.org/10.1007/s00603-012-0276-4.
63. Fell R, Corominas J, Bonnard C, Cascini L, Leroi E, Savage WZ. Guidelines for landslide susceptibility, hazard and risk zoning for land use planning. *Eng Geol*. 2008;102(3–4):85–98. http://dx.doi.org/10.1016/j.enggeo.2008.03.022.
64. Corominas J, Van Westen C, Frattini P, et al *Recommendations for the Quantitative Analysis of Landslide Risk*. Published online; 2014:209–263. http://dx.doi.org/10.1007/s10064-013-0538-8.